Aeroacoustics Conferences
June 4-7, 2024, Rome, Italy
30th AIAA/CEAS Aeroacoustics Conference (2024)

10.2514/6.2024-3324

Assessment of Turbulence Modeling in Navier-Stokes Simulations for Grid-Generated Turbulence and Airfoil Interaction

Sparsh Sharma*, Alexandre Suryadi†, and Michaela Herr‡
Institute of Aerodynamics and Flow Technology, German Aerospace Center (DLR), 38108 Braunschweig, Germany

This paper presents a comprehensive numerical investigation into grid-generated turbulence and its interaction with a NACA0012 airfoil using Large Eddy Simulation (LES). The study is motivated by the need to assess the suitability of this methodology for turbulence interaction noise analysis in aeroacoustic wind tunnel experiments. Grid-generated turbulence, created by a set of carefully configured grids within the wind tunnel, is a well-established method for reproducing essential turbulence characteristics. Additionally, it sets the stage for further exploration of turbulence interaction noise, paving the way for advancements in aeroacoustic research. The paper discusses the experimental setup, including the benchmark Model, boundary layer transition, and the far-field noise measurement setup in the Acoustic Wind Tunnel Braunschweig. The synergy between numerical simulations and experimental data promises valuable insights into grid-generated turbulence and its interaction with airfoils, furthering our understanding of aerodynamic and aeroacoustic phenomena. The study aims to characterize turbulence evolution, validate simulation results against wind tunnel measurements, and assess the impact of grid geometry on turbulence statistics.

I. Nomenclature

LES	=	Large Eddy Simulation
DNS	=	Direct Numerical Simulation
GGT	=	Grid Generated Turbulence
LBM	=	Lattice-Boltzmann Method
RANS	=	Reynolds-Averaged Navier-Stokes
TI	=	Turbulence Intensity
M	=	Mesh size
d	=	Bar width
D	=	Chord length of the airfoil
Re	=	Reynolds number
U_0	=	Free stream velocity
ν	=	Kinematic viscosity
C_s	=	Smagorinsky constant
Δt^*	=	Dimensionless time step
Q	=	Q-criterion
ω_z	=	Spanwise component of vorticity
Tu	=	Turbulence intensity
$E(k)$	=	Energy spectra of streamwise velocity fluctuations
L_p	=	Sound pressure level

II. Introduction

The aerodynamic noise generated by wind turbines has emerged as a pressing environmental concern, receiving significant research attention in recent years. While noise abatement efforts in the aviation industry have long been

*Researcher, German Aerospace Center (DLR), sparsh.sharma@dlr.de
†Researcher, German Aerospace Center (DLR), alexandre.suryadi@dlr.de
‡Senior Researcher, German Aerospace Center (DLR), michaela.herr@dlr.de

a focus, other sectors, like wind energy, increasingly recognize noise as a critical design constraint. Aerodynamic noise is flow-induced noise caused by the interaction of flow structures with the airfoil surface and can be divided into inflow turbulence noise and airfoil self-noise. Inflow turbulence noise, which is the topic of the present paper, results from the interaction of upstream atmospheric turbulence with the leading edge of the airfoil, depending on the atmospheric conditions. This interaction of the airfoil with these turbulent eddies generates unsteady lift, which creates a dipole-like sound source at the leading edge of the airfoil [1]. Numerical simulations can offer higher temporal and spatial resolution and, in specific scenarios, prove more cost-effective than the complexities associated with Model construction and the capabilities of wind tunnels. However, acoustically treated wind tunnels are critical in delving into noise mechanisms and comprehending the underlying flow physics. These facilities provide a controlled environment for detailed investigations, contributing significantly to our understanding of noise generation and radiation mechanisms. While wind tunnels are invaluable for experimental validation and testing, assessing and validating numerical solvers using experimental data is crucial. Combining the strengths of numerical simulations with experimental data not only enhances the accuracy of our analyses but also facilitates a more comprehensive study of the problems at hand. To investigate leading edge noise in wind tunnels, turbulence grids play a pivotal role. These grids are employed within the wind tunnel environment either for the production or reduction of turbulence or for creating or eliminating large-scale velocity or pressure [2].

In recent years, numerical investigations into grid-generated turbulence have gained prominence. Seminal studies by Kang et al. [3] and Djenidi [4] delved into the potential of large-eddy simulations (LES) and the lattice-Boltzmann method (LBM), respectively, for modeling grid-generated turbulence. These foundational works laid the groundwork for further advancements in understanding and simulating this complex phenomenon. Building upon this groundwork, Nagata et al. [5] and Suzuki et al. [6] conducted direct numerical studies (DNS) based on the Navier-Stokes equations to explore turbulent mixing and heat transfer in nearly isotropic grid-generated turbulence (GGT). Additionally, Ertunç et al. [7] conducted DNS using LBM to investigate mixing and homogeneity in GGT. Torrano et al. [8] performed a comparative analysis of experimental and RANS-based studies on grid-generated turbulence decay, establishing the efficacy of different models in varying regions. Liu et al. [9] examined grid-generated turbulence in wind tunnel experiments, revealing promising applications in industrial aerodynamic vibration tests. Song et al. [10] studied the effects of incoming grid-generated turbulence around a cylinder, presenting insights into non-Gaussian characteristics and a bistable flow pattern relevant to ocean engineering. The diverse perspectives converge toward a cohesive understanding of turbulence behavior. In more recent developments in aeroacoustics, Trascinelli et al. [11] utilized the LBM solver PowerFLOW to simulate the interaction of leading-edge grid-generated turbulence, achieving results comparable to the experimental setup conducted by Bowen et al. [12]. Conversely, in hydroacoustics, Wu et al. [13] conducted LES of an underwater rotor ingesting GGT, directly simulating the inflow turbulence induced by the turbulence grids. A summary of the relevant references on the application of numerical methods to study GGT is given in Table 1. The investigation aims to analyze grid-generated turbulence numerically, aiming to replicate the Aeroacoustic Wind Tunnel Braunschweig (AWB) [21] setup. This represents the foundational phase, numerical study, and its comparison with analytical solutions of a broader study focusing on generated turbulence and associated noise generation mechanisms in AWB. Four grids characterized by distinct attributes have been employed to generate turbulent inflow for a NACA0012 airfoil. The utilization of the OpenFOAM LES suite ensures fidelity in the simulation.

The paper is structured with Section III presenting the numerical approach, problem formulation, and computational domain. Section IV discusses the results and cross-comparisons of predictions, and Section V concludes.

III. Flow simulation

A. Numerical approach

In the present paper, LES is used to calculate the near-field sources. In LES, the large eddies of the flow are assumed to be geometry-dependent, while smaller eddies are assumed to be universal. The large eddies can then be directly considered in a calculation by resolving them in a grid, while the small eddies can be indirectly accounted for using a subgrid-scale model (SGS model). The governing equations for LES are derived by applying spatial filtering to the incompressible Navier-Stokes equations. The filtered momentum and continuity equations are

$$\frac{\partial(\bar{u}_i)}{\partial x_i} = 0 \tag{1}$$

Table 1 Relevant literature on the application of numerical methods to study grid-generated turbulence (GGT). This recapitulation is strictly not an exhaustive list.

Author(s)	Year	Approach
Kang et al. [3]	2003	LES
Djenidi et al. [4, 14, 15]	2006,2012,2013	LBM
Nagata et al. [5]	2008	DNS
Suzuki et al. [6]	2010	DNS
Ertunç et al. [7]	2010	LBM
Blackmore et al. [16]	2013	LES
Rieth et al. [17]	2014	LES
Laizet et al. [18]	2015	DNS
Liu et al. [9]	2017	LES
Gorbunova et al. [19]	2020	DNS
Bos [20]	2020	$k-\epsilon$
Song et al. [10]	2022	DNS
Trascinelli et al. [11]	2023	LBM
Wu et al. [13]	2023	LES

and

$$\frac{\partial(\bar{u}_j)}{\partial t} + \frac{\partial(\overline{u_i u_j})}{\partial x_i} = -\frac{1}{\rho}\frac{\partial \bar{p}}{\partial x_j} + \nu \frac{\partial^2 \bar{u}_j}{\partial x_i \partial x_i}, \tag{2}$$

respectively. Here, the summation is applied for repeated indices, and the overbar is used to denote spatially filtered quantities, e.g., $\bar{u}_i$ denotes a filtered velocity field represented as

$$\overline{u}_i(\mathbf{x}, t) = \int G(\mathbf{x,y}) u_i(\mathbf{y}, t) d\mathbf{y}, \tag{3}$$

where $G(\mathbf{x,y})$ is the convolution kernel in physical space unique to the filter function used. Various filter functions are available for the attenuation of high wavenumber modes.

In the above equations, $\bar{p}(x,t)$ is the filtered pressure field. These equations differ from the Navier-Stokes equations because the filtered product $\overline{u_i u_j}$ is different from the product of filtered velocities $\bar{u}_i \bar{u}_j$. The difference is the residual stress tensor (τ_{ij}^R) defined as

$$\tau_{ij}^R = \overline{u_i u_j} - \bar{u}_i \bar{u}_j, \tag{4}$$

which is analogous to the Reynolds stress tensor. The residual kinetic energy is

$$k_r = \frac{1}{2}\tau_{ij}^R, \tag{5}$$

and the anisotropic residual-stress tensor (τ_{ij}^r) is defined as

$$\tau_{ij}^r = \tau_{ij}^R - \frac{2}{3} k_r \delta_{ij}. \tag{6}$$

With these definitions, the filtered momentum equation, Eq. (2), can be rewritten as

$$\frac{\bar{D}\bar{u}_j}{\bar{D}t} = \nu \frac{\partial^2 \bar{u}_j}{\partial x_i \partial x_i} - \frac{1}{\rho}\frac{\partial \bar{p}}{\partial x_j} - \frac{\partial \tau_{ij}^r}{\partial x_i}. \tag{7}$$

Here, the filtered equations for $\bar{u}$ are not yet closed. The closure is achieved by modeling the residual or the subgrid-scale stress tensor τ_{ij}^r. Subgrid-scale turbulence models usually employ the Boussinesq hypothesis [22] and seek to calculate the SGS stress tensor. A standard subgrid-scale model is the Smagorinsky model [23], which constitutes an eddy viscosity model that takes the form

$$\tau^r_{ij} - \frac{1}{3}\tau_{kk}\delta_{ij} = -2\nu_t\bar{S}_{ij}, \quad (8)$$

where ν_t is the turbulent eddy viscosity and $\bar{S}_{ij} = \frac{1}{2}\left(\frac{\partial \bar{u}_i}{\partial x_j} + \frac{\partial \bar{u}_j}{\partial x_i}\right)$ is the rate-of-strain tensor. In the Smagorinsky model, ν_t is modelled as

$$\nu_t = C_s\Delta^2\sqrt{2\bar{S}_{ij}\bar{S}_{ij}} = C_s\Delta^2\left|\bar{S}\right|, \quad (9)$$

where Δ is the grid size, and C_s is a constant. This method assumes that the energy production and dissipation of the small scales are in equilibrium. The Smagorinsky constant C_s is set to 0.167 in OpenFoam [24].

The computational setup involved using the incompressible solver $pimpleFoam$, based on the factorized finite volume method described by Geurts citeGeurts2003. The solver uses a hybrid approach combining the *Pressure-Implicit with Splitting of Operators* (PISO) algorithm and the *Semi-Implicit Method for Pressure-Linked Equations* (SIMPLE) algorithm for pressure-velocity coupling. This combination is implemented following the Rhie and Chow interpolation method for the cell-centered data storage structure as proposed by Issa [25]. A central difference scheme (CDS2) [26] has been used to approximate the convective term contributions calculations. The pressure gradient and all inviscid terms were approximated to fourth-order accuracy. To ensure a local Courant number of less than 1.0, a second-order implicit Eulerian method (BDF-2) [26] was used for time integration, complemented by a dynamically adjustable time-stepping technique. For the solution of linear systems with a local accuracy requirement of 10^{-7} for all dependent variables at each time step, the Incomplete Cholesky Preconditioner (ICCG) [27] was employed. This was achieved using a preconditioned (bi-)conjugate gradient method [28].

In this study, a dimensionless time step $\Delta t^* = \Delta t U_0/D$ of 0.012 was implemented, where Δt represents the physical time step, U_0 the free stream velocity and D the characteristic length, precisely the chord length of the airfoil. This configuration corresponded to a total simulation time of 1.0 seconds, resulting in approximately 400 to 450 time steps per shedding cycle.

B. Problem formulation

This section describes the numerical set-up inspired by the AWB for the grid-generated turbulence and its interaction with the airfoil downstream. The wind tunnel nozzle and the turbulence grid are shown in Fig. 1 and 2. The turbulence grids are strategically placed at two different locations within the AWB wind tunnel: between the nozzle throat and exit, as shown in Fig. 1b, and at the nozzle exit, as shown in Fig. 1c. The rationale for this experimental design is to investigate the effect of the nozzle walls on the generated turbulence, particularly when the turbulence grid is positioned between the nozzle throat and exit. The turbulence grid is characterized by its mesh size (M) and bar width (d), as visually depicted in Fig. 2. In the current investigation, two grids were used, both with the same mesh size but different bar widths. The study examines four different grid configurations using two turbulence grids placed at two locations in the nozzle with a NACA0012 airfoil in the wake of the grid in a subsonic flow, as detailed in Table 2. Table 1 shows four grids with rectangular holes with a mesh width of M mm, and a bar width of d mm is used. The chord length of the airfoil is represented by D, the Reynolds number $Re = DU_0/\nu$ is computed about the chord length D, the incoming flow velocity U_0, and the kinematic viscosity ν.

Table 2 Overview of turbulence grids used in the experiments, parameter definitions in Fig. 1).

Configuration	M (mm)	d (mm)	g(mm)
G1	80	4	500
G2	80	4	1000
G3	80	2	500
G4	80	2	1000

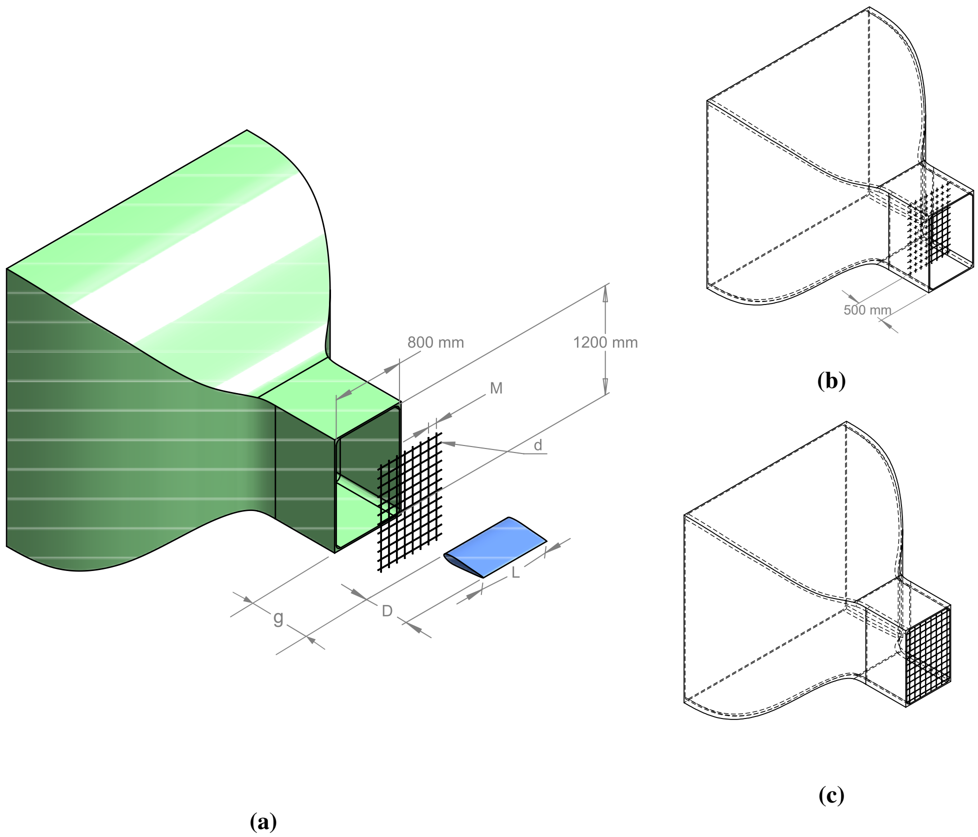

Fig. 1 Schematic illustrating: (a) the contraction nozzle with the turbulence grid and the wing section downstream, (b) the configuration with the grid placed midway between the nozzle exit and throat, and (c) the configuration with the grid placed at the nozzle exit of the Aeroacoustic Wind Tunnel Braunschweig (AWB) [21].

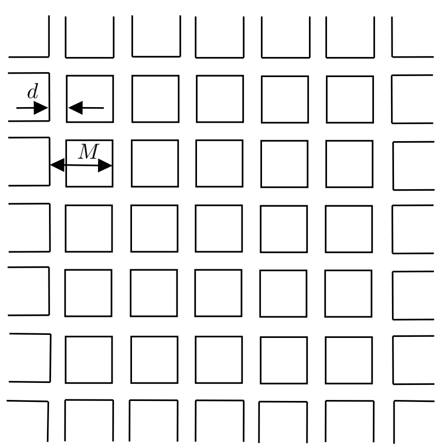

Fig. 2 Schematics of a representative turbulence grid (not to scale).

C. Computational domain

For all four configurations, a three-dimensional computational domain is established, extending six times the airfoil chord length ($6D$) upstream from the leading edge of the airfoil to the velocity inlet boundary and 28 times the chord length ($28D$) downstream to the pressure outlet. The upper and lower boundaries of the domain are defined as symmetry boundaries and are both situated at a distance of $3D$ from the airfoil chord line, as visualized in Fig. 3. The surface of

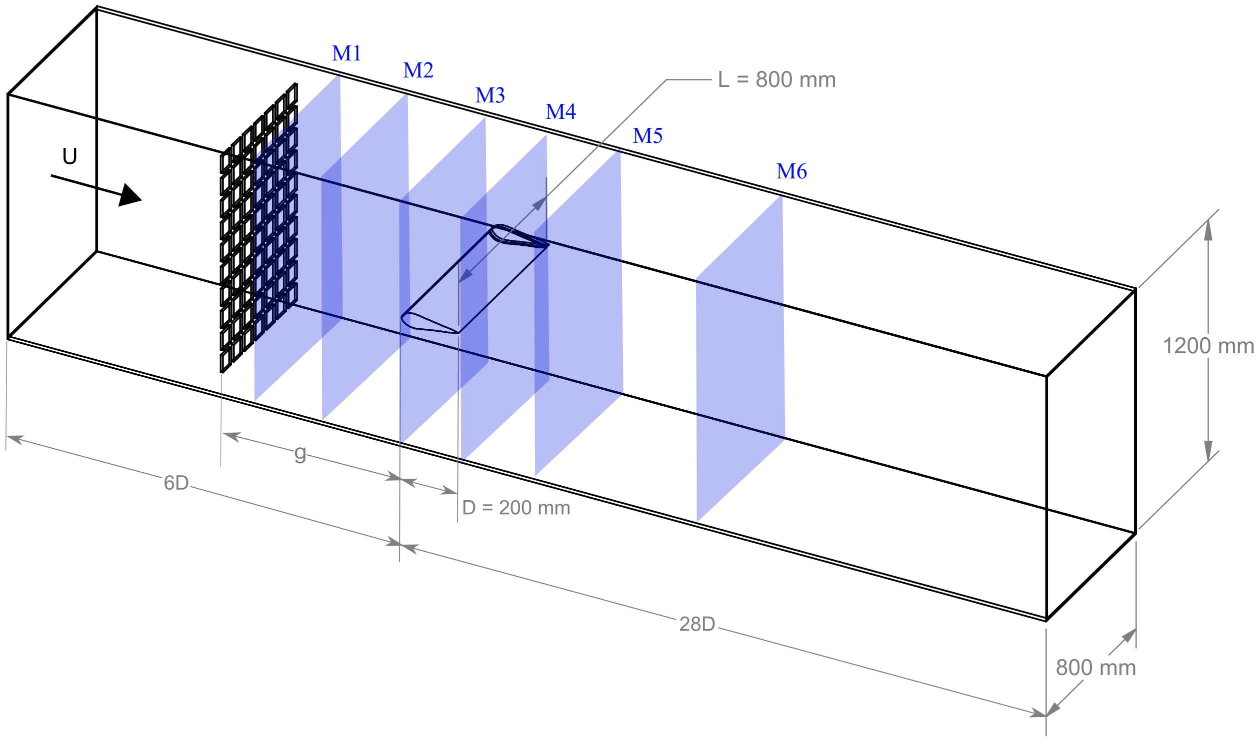

Fig. 3 Computational domain (boundaries and airfoil not to scale).

the airfoil and the turbulence grid is treated as a no-slip wall, and the inflow boundary condition was set to $U_0 = 48$ m/s. A finely resolved mesh was generated near the airfoil wall to accurately resolve the flow within the viscous sublayer, ensuring that the dimensionless wall distance, represented as $y+$, remained less than 1. In the spanwise direction, 100 parallel planes spanning a distance of $4D$ were employed, incorporating periodic boundary conditions. The final computational mesh encompassed 20.6 million cells. Additionally, velocity profiles are extracted from five distinct streamwise positions or planes, identified by labels M1 through M6 in the schematic illustration shown in Fig. 3. Precisely, M1 corresponds to the turbulence grid located midway between the nozzle exit and throat, M2 is at the nozzle exit, M3 represents the leading edge of the airfoil, M4 denotes the trailing edge of the airfoil, and M5 is positioned at a distance of $2D$ from the trailing edge. Moreover, an additional position denoted as M6 is located $10D$ downstream. The primary distinction between the experimental setup and the numerical simulation lies in the absence of the wind tunnel nozzle and the corresponding contraction ratio in the numerical model.

IV. Results

A. Characterization of grid generated turbulence

To understand flow and turbulence characteristics and assess simulation accuracy in resolving grid-generated turbulence, simulations were conducted exclusively with the grid, omitting the airfoil. Turbulence intensity (Tu) was computed as a key metric to capture turbulent flow nature. Simulations progressed from the latest available time (0.1 s), discarding the initial 10000-time steps to remove transients, to a designated end time of 1.0 seconds. A time step (Δt) of 1×10^{-5} seconds ensured temporal accuracy. Velocity field statistics were recorded at four probe stations (M1, M2, M3, and M4) downstream of the exit nozzle, facilitating the examination of turbulence generation and progression.

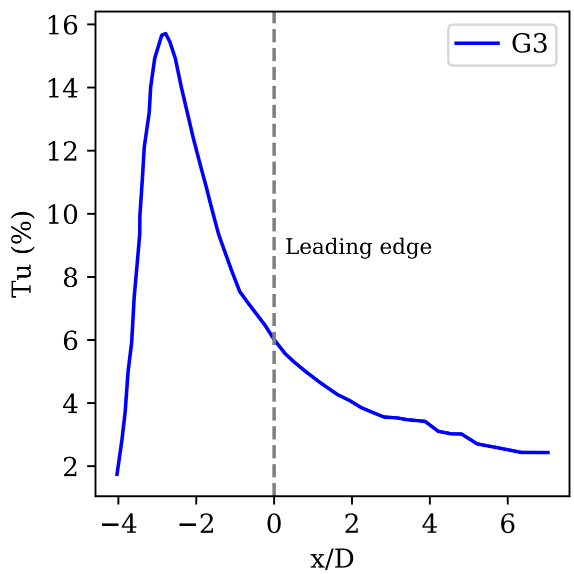

(a)

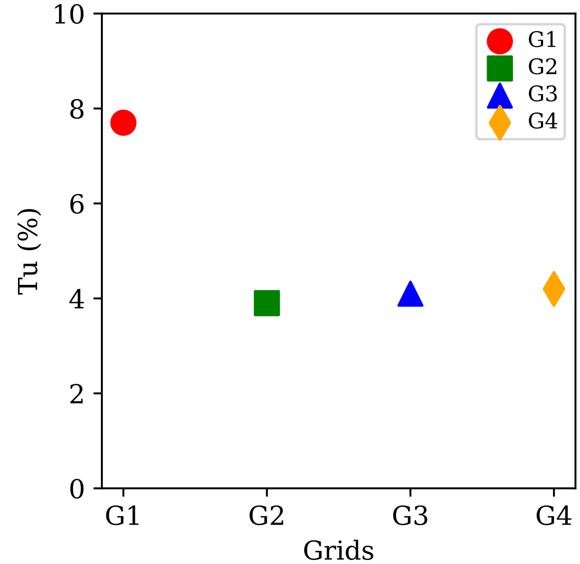

(b)

Fig. 4 (a) Turbulence intensity downstream grid G3 and (b) turbulence intensity of all grids at $x/D = 2$

Turbulence intensity (Tu) was calculated using fluctuating velocity components u', v', w', and the mean flow velocity U:

$$Tu = \frac{1}{U}\sqrt{\frac{1}{3}(u'^2 + v'^2 + w'^2)}. \tag{10}$$

OpenFOAM's `fieldAverage` function object was employed for turbulence intensity computation and other statistical measures like mean values, root mean square (RMS) values, standard deviations (σ), skewness, and kurtosis, calculated at regular 0.0001-second intervals during the simulation.

As the incoming flow is uniform, the turbulence intensities are equal to zero upstream of the turbulence grid, as shown in Fig. 4a for G3. The turbulence intensity rapidly increases near the turbulence grid and decreases as the flow moves downstream. Figure 4b shows the results, indicating that grid G1 has a higher turbulence intensity due to its thicker mesh rod than the other grids. This is consistent with previous studies that indicate that thicker mesh rods in turbulence grids lead to higher turbulence intensities due to increased mean shear and turbulent shear stress [29], surface area, and stronger vortex generation [30], as well as long-distance memory effects [31].

B. Turbulent flow interaction with the wing section

Following preliminary grid-only simulations aimed at extracting turbulence intensity to evaluate the potential for comparing numerical and future experimental setups, the airfoil is positioned downstream of the grid at $x/D = 0$. Figure 5 illustrates the flow structures downstream of the turbulence grid, G3, where the flow structures are shown by the Q-criterion on $Q(D/U)^2 = 1$ iso-surface and colored by the instantaneous normalized vorticity at the end of the simulated time. The wing section is immersed in the incoming vortices. The nozzle walls of configuration G3 are seen to influence the vortical structures downstream of the turbulence grid directly. The structures appear to be elongated relative to the structures right after the walls end and also have extremes of the normalized vorticity magnitude.

Figure 6 the iso-contours of ω_z, z component of the vorticity, taken in the (x, y)-plane. It reveals that the velocity field is likely to be highly inhomogeneous behind the grid to some distance downstream. The map of ω_z indicates that relatively strong coherent vortical structures are generated around the grid elements and interact quickly, as indicated by the division of the iso-contours. Considering that a similar mechanism occurs in the (x, z)-plane, one can easily infer the relatively strong three-dimensional character of the flow behind the grid, resulting in a highly inhomogeneous velocity field. A similar trend has been observed in the numerical studies based on LES [3, 16, 17] and LBM [4, 7].

Figure 7 displays the normalized spanwise vorticity field contours, ω_z, obtained at six monitoring planes in the $(x - y)$ plane, designated M1 to M6 at selected spanwise locations. These contours offer valuable insights into the evolution of the flow. As anticipated, distinct wakes are evident behind the grid, highlighting the intermittent nature of the flow field. Nevertheless, as the distance downstream from the grid bars increases, the flow field transitions towards homogeneity and reduced spatial intermittency. This is attributed to wake interactions and turbulent mixing.

Figure 8 shows the energy spectra, $E(k)$, of streamwise velocity fluctuations downstream of the turbulence grid at $x/D = 10$. Here, k is the longitudinal wavenumber, defined as $k = 2\pi f/U$, where f is the frequency and U is the velocity. It can be observed that $x/D = 10$ corresponds to the early onset of the decay region. The numerical results are compared with the classical Kolmogorov scaling $k^{-5/3}$, which is expected for the inertial subrange. The noisy spectral tails are approximately described but are not physically significant as they indicate limitations by numerical interpolation, random noise, and filtering effects, as previously noted by Djenidi [4]. It is crucial to highlight that the resolution is superior for low wavenumbers at a distance of $x/D = 10$, but it is anticipated to deteriorate further downstream in the high wave numbers.

C. Near- and far field aeroacoustic characteristics

Figure 9 shows numerically obtained spectra of the sound pressure level using Curle's equation simulations and Amiet's analytical theory with Gershfeld's thickness correction [32] and look-up table (LUT) approach based on vortex sound database [33] recorded at a distance of $5D$ and an angle of 90° to the flow (see Fig. 3). The numerically obtained spectrum is calculated by post-processing the time history of the pressure fluctuations over the surface of the airfoil computed using LES. Note that the first 5000 iterations (up to 0.05 s) were not considered while post-processing acoustic and hydrodynamic quantities were used to omit the transient flow phase. In the next step, the time signals were transferred to the frequency range using a Fast Fourier Transform using a Hanning window. The results were then converted to sound pressure levels L_p with a reference pressure of 20 μPa. Validation of the current Curle's implementation is included in Sharma et al. [34, 35]. A unifying factor in all cases is the discrepancy between numerical and analytical results at higher frequencies. This discrepancy can be attributed to the cutoff frequency inherent in the Large Eddy Simulation (LES) method, a factor previously acknowledged in related studies [36] as contributing to spectral mismatch. Consequently, a comprehensive reevaluation of numerical spectra beyond the 2000 Hz is required. Upon closer examination of spectra of G1 and G4 in Fig. 9a and 9d, respectively, it becomes evident that their elevated

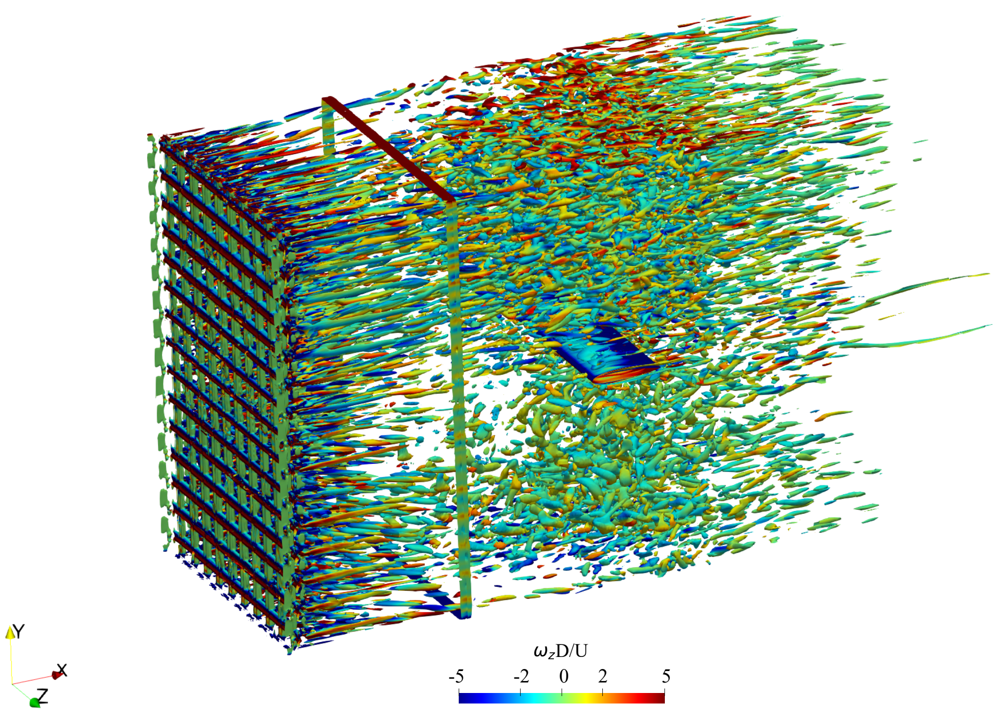

Fig. 5 Iso-surfaces of the vortex structures based on the Q-criterion at Q = 0.5 (colored by the instantaneous normalized vorticity at the end of the simulated time) G3.

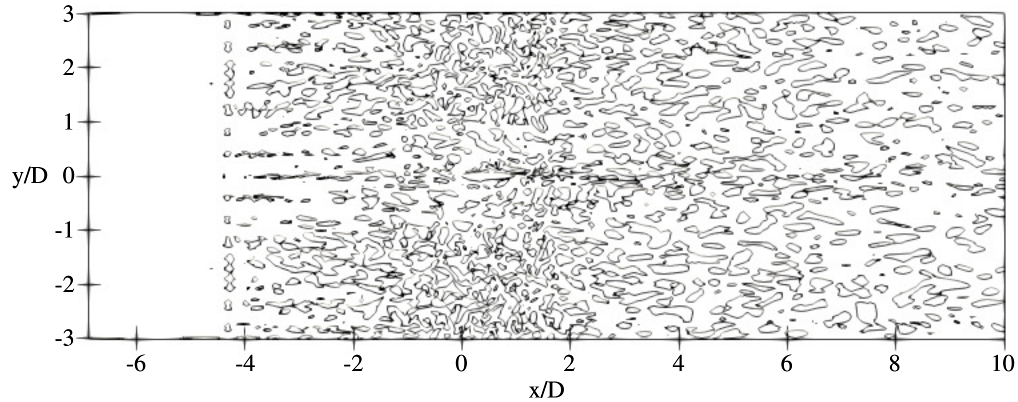

Fig. 6 Iso-surface of the spanwise component of the vorticity, ω_z, in the $(x, y)-$ plane.

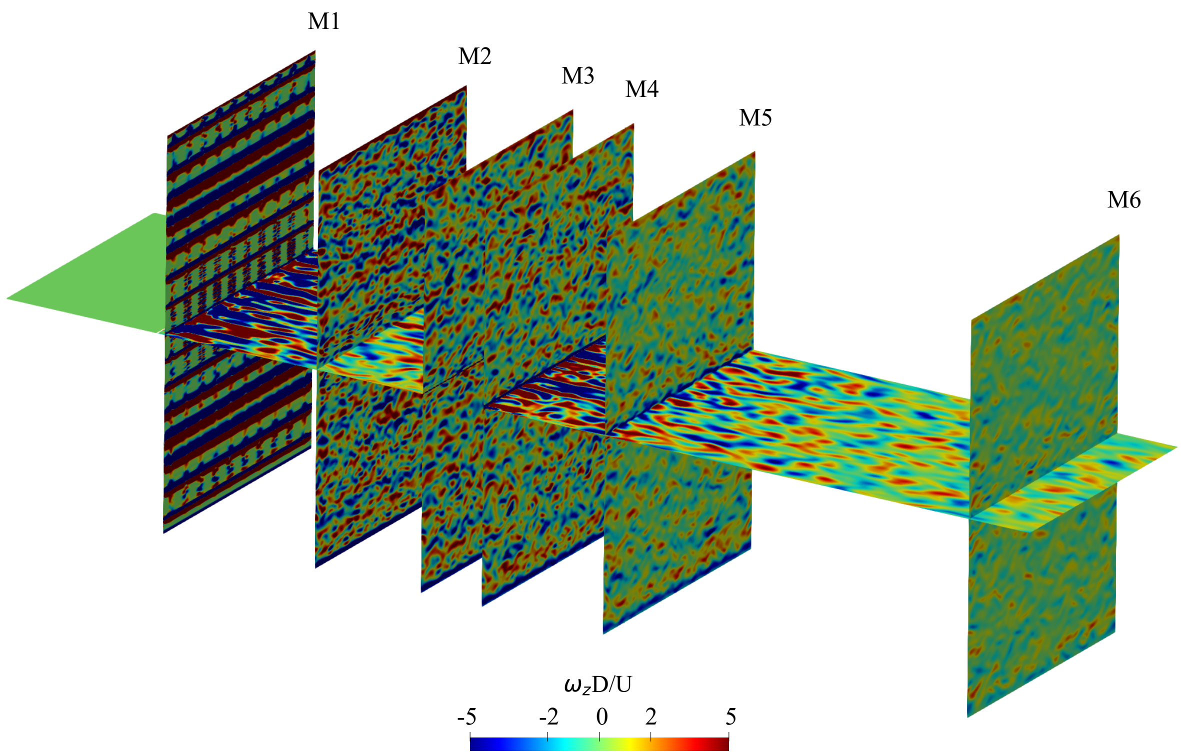

Fig. 7 Contour plots depicting the normalized instantaneous spanwise vorticity field ω_z at M1 through M6.

maximum sound pressure levels are indicative of higher turbulence intensity compared to the remaining grids, as already shown in Fig. 4b.

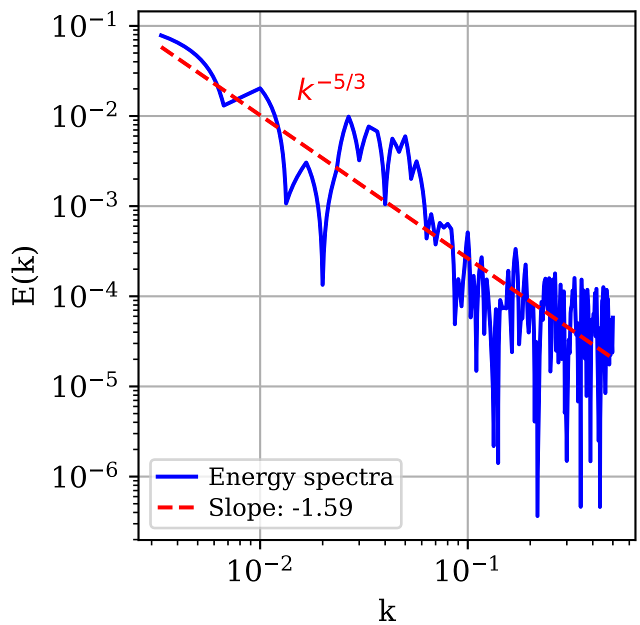

Fig. 8 Energy spectra of streamwise velocity fluctuations $E(k)$. The dashed line indicates the characteristic Kolmogorov scaling $k^{-5/3}$ in the inertial subrange.

V. Conclusion

In conclusion, this study represents the initial phase of a broader investigation of turbulence generation in AWB using turbulence grids. The following conclusions are drawn:

- A workflow to numerically study the turbulence characteristics and noise generation due to its interactions with airfoil using Large Eddy Simulations (LES) and Curle's equation has been successfully created.
- A total of four different configurations of two grids installed at two locations on the nozzle upstream of a NACA0012 wing section was simulated using the approach mentioned above.
- Configuration G1, with larger diameter bars, exhibits higher turbulence intensity, which agrees with the results reported by Cahuzac et al. [36].
- Energy spectra $E(k)$ of streamwise velocity fluctuations downstream of the turbulence grid at $x/D = 10$ demonstrate agreement with classical Kolmogorov scaling $k^{-5/3}$ in the inertial subrange, with noisy spectral tails indicating numerical limitations in high wave numbers due to interpolation and filtering effects.
- Numerical sound pressure level spectra using Curle's equation simulations show discrepancies with analytical results at higher frequencies due to the LES cut-off frequency, requiring reevaluation beyond 2000 Hz. Increased maximum sound pressure levels in grids G1 and G4 indicate higher turbulence intensity than others.

It must be emphasized again that no experimental tests were carried out at this stage. Nevertheless, the numerical simulations of four turbulence grids have provided significant insights into turbulence characteristics and their impact on aerodynamic noise generation. This initial effort lays the groundwork for future experimental investigations, with the results serving as a benchmark for comparison and authentication.

References

[1] Gill, J., Zhang, X., and Joseph, P., "Symmetric airfoil geometry effects on leading edge noise." *The Journal of the Acoustical Society of America*, Vol. 134, 2013, pp. 2669–2680. https://doi.org/10.1121/1.4818769, URL http://www.ncbi.nlm.nih.gov/pubmed/24116405.

[2] Roach, P. E., "The generation of nearly isotropic turbulence by means of grids," *International Journal of Heat and Fluid Flow*, Vol. 8, No. 2, 1987, pp. 82–92. https://doi.org/10.1016/0142-727X(87)90001-4.

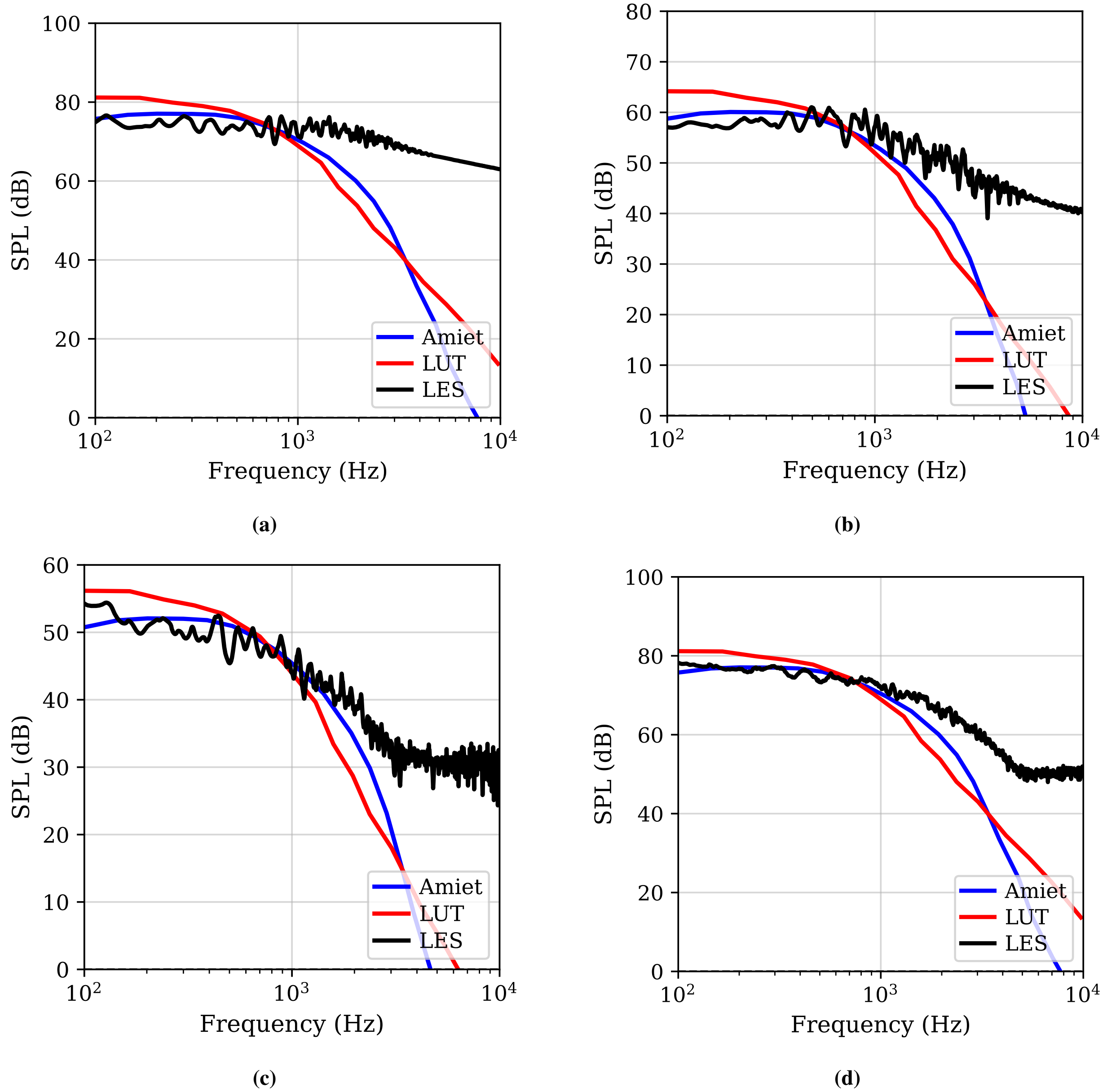

Fig. 9 Comparison between analytical predictions according to Amiet/Gershfeld [32, 37] (—— Amiet), VPM/LUT (—— LUT), and Curle's solution from LES OpenFOAM simulation (—— LES) measured at $\theta = 90°$ for all cases.

[3] Kang, H. S., Chester, S., and Meneveau, C., "Decaying turbulence in an active-grid-generated flow and comparisons with large-eddy simulation," *Journal of Fluid Mechanics*, Vol. 480, 2003, pp. 129–160. https://doi.org/10.1017/S0022112002003579.

[4] Djenidi, L., "Lattice-Boltzmann simulation of grid-generated turbulence," *Journal of Fluid Mechanics*, Vol. 552, 2006, pp. 13–35. https://doi.org/10.1017/S002211200600869X.

[5] Nagata, K., Suzuki, H., Sakai, Y., Hayase, T., and Kubo, T., "Direct numerical simulation of turbulent mixing in grid-generated turbulence," 2008. https://doi.org/10.1088/0031-8949/2008/T132/014054.

[6] Suzuki, H., Nagata, K., Sakai, Y., and Hayase, T., "Direct numerical simulation of turbulent mixing in regular and fractal grid turbulence," *Physica Scripta T*, Vol. T142, 2010. https://doi.org/10.1088/0031-8949/2010/T142/014065.

[7] Ertunç, Ö., Özyilmaz, N., Lienhart, H., Durst, F., and Beronov, K., "Homogeneity of turbulence generated by static-grid structures," *Journal of Fluid Mechanics*, Vol. 654, 2010, pp. 473–500. https://doi.org/10.1017/S0022112010000479.

[8] Torrano, I., Tutar, M., Martinez-Agirre, M., Rouquier, A., Mordant, N., and Bourgoin, M., "Comparison of experimental and RANS-based numerical studies of the decay of grid-generated turbulence," *Journal of Fluids Engineering, Transactions of the ASME*, Vol. 137, No. 6, 2015. https://doi.org/10.1115/1.4029726.

[9] Liu, L., Zhang, L., Wu, B., and Chen, B., "Numerical and experimental studies on grid-generated turbulence in wind tunnel," *Journal of Engineering Science and Technology Review*, Vol. 10, No. 3, 2017, pp. 159–169. https://doi.org/10.25103/jestr.103.21.

[10] Song, B., Ping, H., Zhu, H., Zhou, D., Bao, Y., Cao, Y., and Han, Z., "Direct numerical simulation of flow over a cylinder immersed in the grid-generated turbulence," *Physics of Fluids*, Vol. 34, No. 1, 2022. https://doi.org/10.1063/5.0072730.

[11] Trascinelli, L., Bowen, L., Piccolo, A., Avallone, F., Zamponi, R., Ragni, D., Zang, B., and Zhou, B. Y., "Numerical Simulation of Grid-Generated Turbulence Interaction with a NACA0012 Airfoil," American Institute of Aeronautics and Astronautics (AIAA), 2023. https://doi.org/10.2514/6.2023-3633.

[12] Bowen, L., Celik, A., Azarpeyvand, M., and da Silva, C. R., "Grid Generated Turbulence for Aeroacoustic Facility," *AIAA Journal*, Vol. 60, 2022, pp. 1833–1847. https://doi.org/10.2514/1.J060851.

[13] Wu, J., Yangzhou, J., Ma, Z., and Huang, X., "Numerical study of rotor unsteady forces and noise due to ingestion of grid-generated turbulence," *Physics of Fluids*, Vol. 35, No. 1, 2023. https://doi.org/10.1063/5.0132975.

[14] Djenidi, L., and Tardu, S. F., "On the anisotropy of a low-Reynolds-number grid turbulence," *Journal of Fluid Mechanics*, Vol. 702, 2012, pp. 332–353. https://doi.org/10.1017/jfm.2012.179.

[15] Djenidi, L., Tardu, S. F., and Antonia, R. A., "Relationship between temporal and spatial averages in grid turbulence," *Journal of Fluid Mechanics*, Vol. 730, 2013, pp. 593–606. https://doi.org/10.1017/jfm.2013.351.

[16] Blackmore, T., Batten, W. M., and Bahaj, A. S., "Inlet grid-generated turbulence for large-eddy simulations," *International Journal of Computational Fluid Dynamics*, Vol. 27, 2013, pp. 307–315. https://doi.org/10.1080/10618562.2013.819972.

[17] Rieth, M., Proch, F., Stein, O. T., Pettit, M. W., and Kempf, A. M., "Comparison of the Sigma and Smagorinsky LES models for grid generated turbulence and a channel flow," *Computers and Fluids*, Vol. 99, 2014, pp. 172–181. https://doi.org/10.1016/j.compfluid.2014.04.018, URL http://dx.doi.org/10.1016/j.compfluid.2014.04.018.

[18] Laizet, S., Nedić, J., and Vassilicos, J. C., "The spatial origin of -5/3 spectra in grid-generated turbulence," *Physics of Fluids*, Vol. 27, 2015. https://doi.org/10.1063/1.4923042.

[19] Gorbunova, A., Balarac, G., Bourgoin, M., Canet, L., Mordant, N., and Rossetto, V., "Analysis of the dissipative range of the energy spectrum in grid turbulence and in direct numerical simulations," *Physical Review Fluids*, Vol. 5, 2020. https://doi.org/10.1103/PhysRevFluids.5.044604.

[20] Bos, W. J., "Production and dissipation of kinetic energy in grid turbulence," *Physical Review Fluids*, Vol. 5, 2020. https://doi.org/10.1103/PhysRevFluids.5.104607.

[21] Pott-Pollenske, M., and Delfs, J., *Enhanced Capabilities of the Aeroacoustic Wind Tunnel Braunschweig*, ???? https://doi.org/10.2514/6.2008-2910.

[22] Pope, S. B., *Turbulent Flows*, Cambridge Univ. Press, 2000.

[23] Smagorinsky, J., "General circulation experiments with the primitive equations: I. The basic experiment," *Mon. Weather Rev.*, Vol. 91, No. 3, 01 Mar. 1963, pp. 99 – 164. https://doi.org/10.1175/1520-0493(1963)091<0099:GCEWTP>2.3.CO;2.

[24] Weller, H. G., Tabor, G., Jasak, H., and Fureby, C., "A tensorial approach to computational continuum mechanics using object-oriented techniques," *Computers in Physics*, Vol. 12, 1998, pp. 620–631. https://doi.org/10.1063/1.168744.

[25] Issa, R. I., "Solution of the implicitly discretised fluid flow equations by operator-splitting," *J. Comput. Phys.*, Vol. 62, No. 1, 1986, pp. 40–65. https://doi.org/https://doi.org/10.1016/0021-9991(86)90099-9.

[26] Geurts, B. J., *Elements of direct and large-eddy simulation*, 2003.

[27] Jacobs, D. A. H., "Preconditioned Conjugate Gradient Methods for Solving Systems of Algebraic," , 1981.

[28] Hestenes, M. R., and Stiefel, E., "Methods of conjugate gradients for solving linear systems," *J. Res. Natl. Bur. Stand.*, Vol. 49, No. 6, 1952, p. 409. https://doi.org/https://doi.org/10.6028/jres.049.044.

[29] Rose, M. E., *Elementary Theory of Angular Momentum*, Wiley, New York, 1957.

[30] Vita, G., Hemida, H., Andrianne, T., and Baniotopoulos, C., "Generating atmospheric turbulence using passive grids in an expansion test section of a wind tunnel," *Journal of Wind Engineering and Industrial Aerodynamics*, 2018. https://doi.org/10.1016/J.JWEIA.2018.02.007.

[31] Hinze, J., and Builtjes, P., "Rotation of the Reynolds' stress tensor in a decaying grid-generated turbulent flow," *Physics of Fluids*, Vol. 20, 1977. https://doi.org/10.1063/1.861727.

[32] Gershfeld, J., "Leading edge noise from thick foils in turbulent flows," *J. Acoust. Soc. Am.*, Vol. 116, No. 3, 2004, pp. 1416–1426. https://doi.org/https://doi.org/10.1121/1.1780575.

[33] Sharma, S., Sarradj, E., and Schmidt, H., "Stochastic modelling of leading-edge noise in time-domain using vortex particles," *J. Sound Vib.*, Vol. 488, 2020, p. 115656. https://doi.org/https://doi.org/10.1016/j.jsv.2020.115656.

[34] Sharma, S., Geyer, T. F., and Arcondoulis, E. J., "On the influence of porous coating thickness and permeability on passive flow and noise control of cylinders," *Journal of Sound and Vibration*, Vol. 549, 2023, p. 117563. https://doi.org/10.1016/j.jsv.2023.117563.

[35] Sharma, S., Geyer, T. F., and Giesler, J., "Effect of geometric parameters on the noise generated by rod-airfoil configuration," *Applied Acoustics*, Vol. 177, 2021, p. 107908. https://doi.org/10.1016/j.apacoust.2021.107908.

[36] Cahuzac, A., Boudet, J., Borgnat, P., and Lévêque, E., "Smoothing algorithms for mean-flow extraction in large-eddy simulation of complex turbulent flows," *Physics of Fluids*, Vol. 22, No. 12, 2010, p. 125104. https://doi.org/10.1063/1.3490063, URL https://doi.org/10.1063/1.3490063.

[37] Amiet, R. K., "Acoustic radiation from an airfoil in a turbulent stream," *J. Sound Vib.*, Vol. 41, No. 4, 1975, pp. 407–420. https://doi.org/https://doi.org/10.1016/S0022-460X(75)80105-2.